Applied Materials Today 4 (2016) 24–30

Contents lists available at ScienceDirect

Applied Materials Today

journal homepage: www.elsevier.com/locate/apmt

Thickness of functionalized graphene oxide sheets plays critical role in tissue accumulation and urinary excretion: A pilot PET/CT study

Dhifaf A. Jasim[a,b], Herve Boutin[c,d], Michael Fairclough[c], Cécilia Ménard-Moyon[e], Christian Prenant[c], Alberto Bianco[e], Kostas Kostarelos[a,b,*]

[a] Nanomedicine Lab, School of Medicine, Faculty of Medical and Human Sciences, University of Manchester, AV Hill Building, Manchester, United Kingdom
[b] National Graphene Institute, University of Manchester, Manchester, United Kingdom
[c] Wolfson Molecular Imaging Centre, University of Manchester, Manchester, United Kingdom
[d] Faculty of Medical and Human Sciences, Institute of Population Health, University of Manchester, Manchester, United Kingdom
[e] CNRS, Institut de Biologie Moléculaire et Cellulaire, Laboratoire d'Immunopathologie et Chimie Thérapeutique, CNRS-UPR3572, 67000 Strasbourg, France

ARTICLE INFO

Article history:
Received 20 December 2015
Received in revised form 8 April 2016
Accepted 26 April 2016

Keywords:
Pharmacology
Pharmacokinetics
Carbon
Imaging
Nanomedicine

ABSTRACT

We have recently reported that administration of thin graphene oxide (GO) sheets in the systemic circulation of rodents leads to rapid urinary excretion for the majority of injected dose and accumulation by the reticuloendothelial system organs for the remaining dose. In this study, graphene oxide was functionalized with a chelating moiety (DOTA, (1,4,7,10-tetraazacyclododecane-1,4,7,10-tetraacetic acid)) and labeled with [^{64}Cu] for positron emission computed tomography (PET/CT) imaging. The thin functionalized graphene oxide material (*f*-GO-thin) consisted of a few layers (~5 nm) in thickness. Aging of the *f*-GO-thin material led to re-stacking of the flakes that resulted in materials of increased thickness (*f*-GO-thick) without altering their lateral dimension. These two types of *f*-GOs were comparatively studied pharmacologically to reveal the previously unexplored *in vivo* role of graphene oxide sheet thickness. Our results showed that a significantly larger fraction of the thicker GO sheets (47.5% of injected dose) remained within the body of living animals 24 h after intravenous administration, residing mainly in the spleen and liver. The thinner GO sheets were predominantly (76.9% of injected dose) excreted through the glomerular filter into the urine. This pilot study provides an initial correlation between graphene-based material structure and pharmacological profile that is imperative towards understanding of how 2D structures behave *in vivo* to give information on potential biomedical applications.

1. Introduction

Graphene has attracted a lot of interest recently due to its unique 2D carbon geometry that offers a variety of outstanding physicochemical properties [1,2]. These properties are explored in diverse scientific disciplines and application areas, ranging from physics to materials science and biology [3–7]. Among the characteristics relevant to biomedical applications of graphene and 2D materials are the large surface area [8–10], high mechanical strength [11–14] and flexibility [3,6] that play critical roles in determining their interactions with soft biological matter [12,15]. Graphene oxide (GO), the oxidation reaction product of various graphitic forms, is rich in oxygen groups on both sides of the planar 2D structure making the material significantly more hydrophilic. As a more biologically-compatible material compared to pristine graphene, GO has generally widened the use of graphene-based materials (GBMs) in biological research and applications [4].

Because of the potential GBMs hold in biomedical applications, it is imperative to understand the fundamental pharmacological interactions of free suspensions of 2D flakes of GO with biological matter at different scales (molecular, cellular, tissue) [15]. GO has been administered in live animal models using different routes of injection, including intravenous [16–19], intraperitoneal [20,21], oral [21] and intravitreal [22] with no reported adverse reactions even after relatively long exposure times [21,22]. After intravenous or intraperitoneal administration, some studies reported the accumulation of GO in tissues of the reticuloendothelial system, followed by slow clearance from those organs over time starting after 24 h from mediastinal lymph nodes [23] or much more rapidly *via* urinary excretion [18]. Urinary excretion within the first few

* Corresponding author at: Nanomedicine Lab, School of Medicine, Faculty of Medical and Human Sciences, University of Manchester, AV Hill Building, Manchester, United Kingdom.
E-mail address: kostas.kostarelos@manchester.ac.uk (K. Kostarelos).

http://dx.doi.org/10.1016/j.apmt.2016.04.003
2352-9407/

hours after intravenous administration of GO has been recently reported [18,24–26], even for GO sheets that are as large as 1 μm in lateral dimension, that is significantly above the dimensions of the glomerular filtration slits (40 nm) [27]. On the other hand, pulmonary instillation of pristine graphene, GO or reduced GO (rGO) has been associated with lung retention and activation of acute and chronic inflammatory pathways that may eventually lead to lung injury [23,28,29]. The lung has been identified as a critical organ based on various studies after administration of GO *via* different routes. We believe the reported pulmonary accumulation is mainly due to the poor quality of the GO suspensions administered and their colloidal instability or aggregated state (particularly *in vivo*) that can result in entrapment within the pulmonary capillaries [30]. Accurate control of graphene sheet thickness remains challenging even for materials fabricated by chemical vapour deposition (CVD) [31]. We serendipitously observed that ageing of the thin, covalently functionalized GO (*f*-GO) sheets previously studied [27] was evolving by re-stacking of individual sheets. In the present study, we compared aged (kept over 18 months at 4 °C) DOTA-GO flakes that consisted of a significantly thicker population of flakes compared to freshly synthesized thin DOTA-GO, with apparent unaltered size distributions. These two types of materials were radiolabeled using ^{64}Cu to perform whole body positron emission computed tomography (PET/CT) imaging and pharmacokinetics analysis in mice following intravenous administration. This allowed us to interrogate the previously unexplored effect of GBM thickness on the *in vivo* behavior of functionalized graphene oxide flakes.

2. Experimental

2.1. Synthesis of the graphene oxide (GO)

GO was prepared from Chinese flake graphite (Branwell) by the modified Hummers method [27,32] Briefly, 0.4 g of graphite were mixed with 0.2 g of sodium nitrate ($NaNO_3$), and then 9.2 mL of 99% sulfuric acid (H_2SO_4) was added slowly to the mixture, which was continuously stirred. The temperature did not exceed 20 °C by using an ice bath. After obtaining a homogenized mixture, 1.2 g of potassium permanganate ($KMnO_4$) was added slowly. The temperature was monitored again and did not exceed 20 °C. The mixture was then removed from the ice bath and the temperature started to rise gradually. This was maintained for 30 min until the mixture started thickening and became a paste of dark brown/green color. Deionized H_2O was added slowly while stirring at the same time. Violent effervescence and rapid increase of temperature was observed. Temperature was monitored and was kept between 98–100 °C for another 30 min with the aid of a hot plate. The mixture was further diluted with 56 mL of deionized H_2O and 6 mL 30% H_2O_2 was added gradually for the reduction of the residual $KMnO_4$, MnO_2 and Mn_2O_7 to soluble manganese sulfate ($MnSO_4$) salts. The resulting suspension was centrifuged at 9000 rpm for 20 min and the supernatant was discarded. This was repeated until the supernatant had a pH of about 6 and the GO gel-like layer appeared on top of the oxidation byproducts. This layer was then extracted using warm water carefully in order to avoid remixing of this layer with graphite oxide sediments.

2.2. Preparation of the functionalized graphene oxide (f-GO)

f-GO was prepared according to the protocol reported in a previous work [27]. The formation *f*-GO-thick was observed spontaneously from *f*-GO-thin by an aging effect after 1.5 years of the fresh preparation.

2.3. Radiolabeling of f-GO

f-GO–thin, *f-GO*-thick and control EDTA (ethylenediaminetetraacetic acid) were radiolabeled as previously described [27,33]. All samples were diluted with an equal volume of 0.2 M ammonium acetate buffer at pH 5.5. Then 20 MBq of $^{64}CuCl_3$ was added. The copper was left to react with the samples for 60 min at 60 °C, after which the reaction was quenched by the further addition of 0.1 M EDTA chelating solution.

2.4. Radiolabeling efficiency of f-GO

The labeling efficiency was determined by taking aliquots of each final product, then diluting them five folds in PBS. One μL was spotted on silica gel impregnated glass fibre sheets (PALL Life Sciences, UK). The strips were developed with a mobile phase of 50 mM EDTA in 0.1 M ammonium acetate and allowed to dry before analysis. This was then developed and the autoradioactivity quantitatively counted using a Scan-RAM Radio TLC detector (LabLogic, UK). The immobile spot on the TLC strips indicated the percentage of radiolabeled *f*-GO material, while free [^{64}Cu]-EDTA were seen as the mobile spots near the solvent front.

2.5. Scanning electron microscopy (SEM)

SEM imaging was performed using an FEI Quanta 250 ESEM operating in high vacuum. GO and *f*-GO samples dispersed in water were further diluted prior to pipetting onto super smooth SEM mounts (silicon wafer chips) and allowed to dry prior to examination by SEM.

2.6. Atomic force microscopy (AFM)

A Bruker Multimode 8 was used in tapping-mode with an J-type scanner, Nanoscope VI controller, Nanoscope v614r1 control software (Veeco, Cambridge, UK) and a silicon tapping tip (NSG01, NTI-Europe, Apeldoorn, The Netherlands) of 10 nm curvature radius, mounted on a tapping mode silicon cantilever with a typical resonance frequency 283–374 kHz and a force constant of 12–103 N/m (Bruker OTESPA, UK). Images were taken in air, by depositing 40 μL of the sample on a freshly cleaved mica surface (Agar Scientific, Essex, UK) coated with poly-L-lysine 0.01% (Sigma-Aldrich, UK) and allowed to adsorb for 2 min. Excess unbound material was removed by washing with filtered distilled water, and then allowed to dry in air; this step was repeated once. Size distributions were carried out using ImageJ software, to measure the lateral dimension of individual graphene sheets. Sheet thickness distribution was determined from AFM height sections. Both size and thickness distributions were based on counting approximately 81–246 individual sheets.

2.7. Raman spectroscopy of GO and f-GO

Samples were prepared for analysis by drop casting approximately 20 μL of *f*-GO dispersion on to a glass slide. Samples were left to dry at 37 °C. Spectra were collected using a micro-Raman spectrometer (Thermo scientific, UK) using a λ = 633 nm LASER. Spectra were collected at a laser power of 0.4 mW at a magnification lens of 50 × with 10 s exposure time, averaged over 3 locations.

2.8. Animal handling procedures

Eight week-old C57BL/6 mice each weighing between18.1 ± 0.7 g were obtained from Harlan (Oxfordshire, UK), allowed to acclimatize for 1 week and kept under a 12 h light/dark cycle under steady temperature and humidity with

access to food and water *ad libitum*. All experiments were conducted with prior approval from the UK Home Office. One mouse was used for each imaging experiment.

2.9. Positron emission computed tomography (PET/CT)

Mice were anesthetized using isoflurane (induction 5%, 2–2.5%) in O_2 and catheterized in the tail vein for tracer administration. Each animal was injected *via* the tail vein with 200 μL containing 50 μg of *f*-GO labeled with 2.51–4.55 MBq of [^{64}Cu]. At different time points after injection (1, 3.5 and 24 h), mice were imaged on a Siemens Inveon® PET/CT scanner. Mice were first scanned for 60 min scans starting with the administration of the tracer. Animals were then allowed to recover and re-anesthetized and rescanned for 30 min, 3 h and 24 h post-injection. Animal respiration and temperature were controlled using a pressure-sensitive pad and rectal probe (BioVet, m2 m Imaging Corp., Cleveland, OH, USA) and body temperature was maintained at 37 ± 0.7 °C *via* the interface managed by the BioVet system. PET/CT was performed as previously described [34]. Briefly, a CT scan was performed prior to the PET acquisition for attenuation correction. The list mode emission data were histogrammed into 25 dynamic frame 3D sonograms for the 1 h scans and into a single 30 min frame for the 3 h and 24 h scans. Scans were normalized, corrected for dead-time, attenuation, scatter and radioactive decay, and reconstructed using OSEM3D (16 subsets and 4 iterations) into images of dimensions 128 × 128 × 159 voxels of volume 0.776 × 0.776 × 0.796 mm^3.

2.10. PET image analysis

PET images were analyzed using the BrainVisa/Anatomist framework (http://brainvisa.info/). Briefly, PET were segmented using the Local Means Analysis (LMA) method (http://www.ncbi.nlm.nih.gov/pubmed/18334430) with Partial Volume Effect (PVE) correction using the Geometric Transfer Matrix (GTM) method and the ROIopt methods (http://www.ncbi.nlm.nih.gov/pubmed/18334430, http://www.ncbi.nlm.nih.gov/pubmed/20942812, http://www.ncbi.nlm.nih.gov/pubmed/20443471). Automatic segmentation of the volume had the advantage of producing user-independent ROIs, these ROIs were then checked for consistency in size and position for the organs measured in the co-registered CT images.

3. Results

3.1. Preparation and characterization of GO

GO was prepared by the modified Hummers' method described previously [27,32] using chemical oxidation in strong acidic conditions and collecting only the top layer of multiple centrifugation/filtration purification cycles. This resulted in highly purified graphene oxide sheets stably dispersed in an aqueous phase at physiological pH. Structural characterization of the GO is shown in Fig. 1A and Fig. S1A. The SEM and AFM images on the left hand side of Fig. 1A show the morphology and ultrathin nature of the GO prepared. AFM height images in Fig. S1A were further analyzed by counting 81 and 142 individual sheets to obtain the thickness and lateral size distributions respectively, as shown in Fig. 1A (right). The thickness of as-prepared GO sheets ranged between 1 and 2 nm corresponding to 2–4 single sheets of graphene, while the lateral dimension of the sheets broadly ranged from 200 nm and to 2 μm. Fig. S2 displays the Raman spectrum showing the characteristic G and D bands of the GO with I_D/I_G intensity ratio.

3.2. Synthesis and characterization of thin, functionalized graphene oxide (f-GO-thin)

To synthesize the thin functionalized *f*-GO-thin, the chelating agent DOTA was grafted onto GO, as previously described [27]. Briefly, triethylene glycol (TEG) diamine was used to open the epoxy rings and introduce amino functions on the GO surface. The amount of amino groups on GO-NH_2 was assessed by the Kaiser test [35]. The loading corresponded to 595 μmol of NH_2 functions per gram of GO. Then, the amino groups of GO-NH_2 were derivatized with DOTA bearing an isothiocyanate moiety (DOTA-NCS). Kaiser test of *f*-GO-DOTA indicated that the amount of unreacted amine functions was 230 μmol/g, accounting for a ~60% coupling efficiency.

Structural characterization of the freshly prepared *f*-GO-thin is shown in Fig. 1B and Fig. S1B. The SEM and AFM images in Fig. 1B show the lateral morphology and thickness of the functionalized GO sheets. AFM height images in Fig. S1B were further analyzed by counting 246 and 149 individual sheets to obtain the thickness and lateral size distribution, respectively. The *f*-GO-thin was found to range between 4 and 8 nm in thickness indicating that the functionalization reaction and processing led to few-layered sheets. The distribution in lateral size after functionalization was reduced to sheets no larger than 0.8 μm compared to the starting GO, in agreement with our previous findings [27]. The Raman spectrum with I_D/I_G ratio of *f*-GO-thin is displayed in Fig. S2.

3.3. Aging and characterization of thick, functionalized (f-GO-thick)

The ageing of GO-DOTA materials was monitored to reveal that stacking of the individual flakes was taking place, leading to increased overall thickness of the aged GO flakes. To that end, following the synthesis of *f*-GO-thin, the material was kept dispersed in water at 4 °C for 18 months. The thin GO sheets gradually re-stacked forming the aged, thicker material. Structural characterization of *f*-GO-thick (Fig. 1C and Fig. S1C), by SEM and AFM imaging confirmed the increased thickness of the aged functionalized sheets. AFM height images in Fig. S1C were further analyzed by counting 167 and 123 individual sheets to obtain the thickness and lateral size distribution respectively. The *f*-GO-thick sheets were shown to be four times thicker than the starting *f*-GO-thin material, with flakes about 20 nm thick on average (up to 40–50 nm thick), while their lateral size distribution remained unchanged (up to 0.8 μm) compared to the fresh *f*-GO-thin. The Raman spectrum with I_D/I_G ratio of *f*-GO-thick is displayed in Fig. S**2**.

3.4. Radiolabeling and PET/CT imaging f-GO-thin and f-GO-thick

The two *f*-GO-DOTA aqueous suspensions were then radiolabeled using $^{64}CuCl_3$ by using the heating method described previously [27,33]. The efficiency of radiolabeling of the two functionalized GO samples with [^{64}Cu] (*f*-GO-thin and *f*-GO-thick) compared to control EDTA are shown in Fig. S3. The radiolabeling efficiency of freshly prepared [^{64}Cu]-*f*-GO-thin was more than double that of the [^{64}Cu]-*f*-GO-thick (62.7% *vs* 26.4%), while the control sample [^{64}Cu]-EDTA almost entirely moved to the solvent front (89.7%), as expected. That indicated that less DOTA groups were available for radiolabeling in the thicker samples, indirectly confirming the stacking process that took place. Intravenous injection of the same amount of thin and thick radiolabeled GO sheets followed by dynamic PET/CT imaging was then performed. PET imaging-based comparative pharmacokinetics and tissue distribution profiling of [^{64}Cu]-*f*-GO-thin, [^{64}Cu]-*f*-GO-thick and control [^{64}Cu]-EDTA using PET/CT imaging was carried out (Fig. 2, Fig. S4). PET imaging in the heart and brain suggested

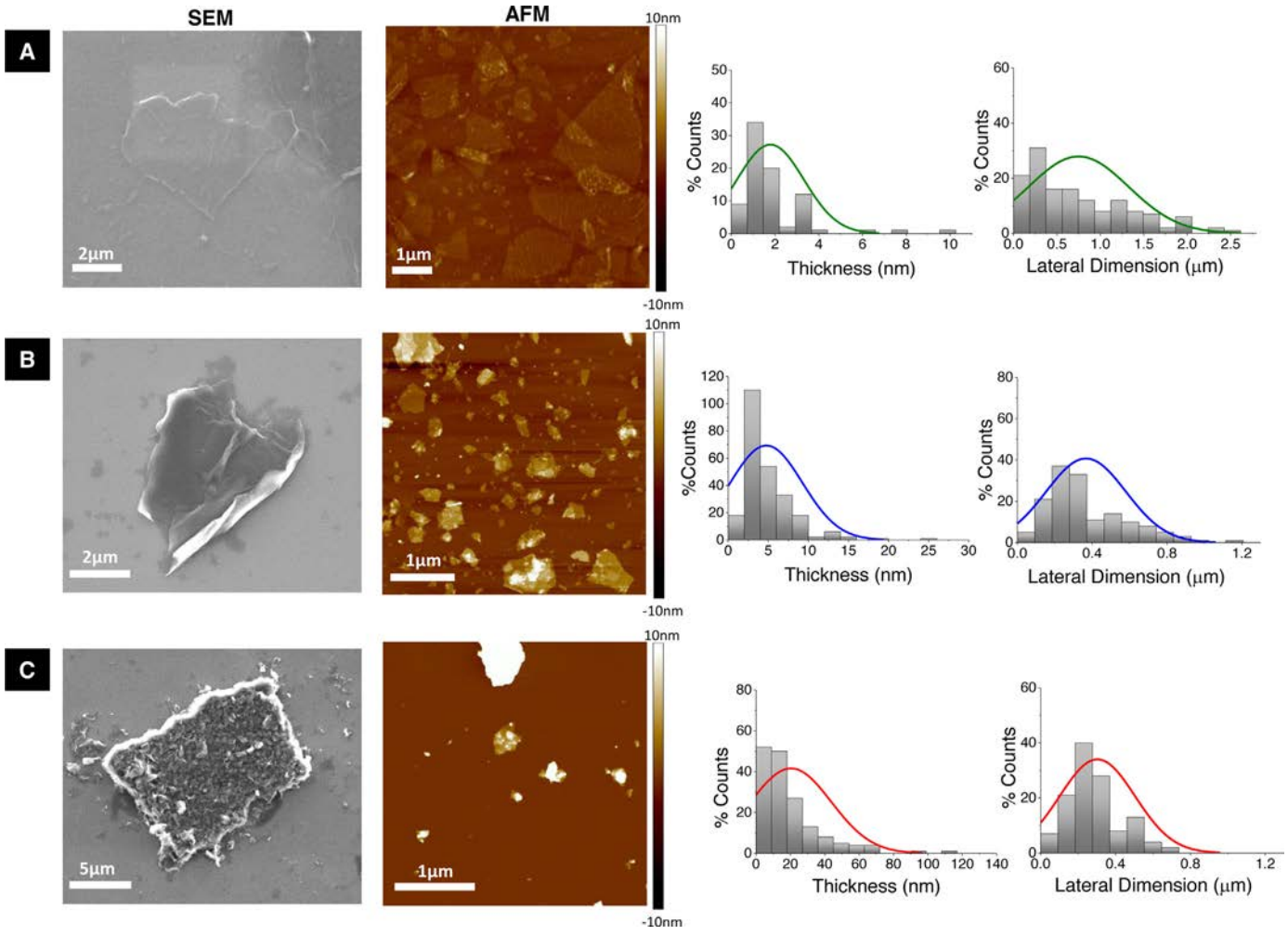

Fig. 1. Structural characterization of GO, *f*-GO and aged *f-GO*. SEM and AFM images of: (A) GO; (B) *f*-GO-thin; and (C) *f*-GO-thick. Thickness and lateral size distribution analysis were performed based on counting several (81–246) individual sheets from the AFM images.

fast perfusion-dependent kinetics of the GO sheets, peaking at 30–40 s post-injection and rapidly decreasing, with no significant accumulation in both those organs (Fig. S4). Very different tissue distribution and accumulation profiles were observed for [^{64}Cu]-*f*-GO-thin, [^{64}Cu]-*f*-GO-thick and control [^{64}Cu]-EDTA (Fig. 2, Table S1 and Video S1). Namely, [^{64}Cu]-*f*-GO-thick began accumulating rapidly (within 1 min post-injection) in the liver and spleen. Almost equally rapid pharmacokinetics (peak levels and wash-out within 5 min post-injection) and much lower accumulation were observed through the kidneys and lungs. Conversely, the PET signal from [^{64}Cu]-*f*-GO-thin increased more slowly in kidneys (peak at 10 min post-injection) but to much higher levels, followed by rapid decrease to reach a plateau within 30–60 min. In terms of tissue distribution and accumulation, the fraction of [^{64}Cu]-*f*-GO-thin that remained in the body of the animals also accumulated mainly in the liver and spleen, followed by a much smaller fraction in the lungs.

It must be noted that at 40–60 min post-injection the levels of tissue retention for the [^{64}Cu]-*f*-GO-thin and [^{64}Cu]-*f*-GO-thick material in the spleen, liver, lung and kidneys were very different. [^{64}Cu]-*f*-GO-thick generally exhibited significantly higher levels of retention in the liver, lungs and particularly the spleen, accompanied by dramatically lower urinary excretion. The urinary excretion observed for [^{64}Cu]-*f*-GO-thick was about half of the levels of urinary excretion obtained for [^{64}Cu]-*f*-GO-thin (Table S1 and Video S1). In the lungs, accumulation was identical for both GO materials (1.6% ID/cm^3 *vs* 1% ID/cm^3 at 40–60 min and 2.5% ID/cm^3 *vs* 0.90% ID/cm^3 at 3.5 h). In the kidneys, the pharmacokinetic profile of [^{64}Cu]-EDTA and [^{64}Cu]-*f*-GO-thin was very similar for both compounds, slowly reaching its maximum 6–7 min post-injection before slowly decreasing to similar levels (0.8%ID/cm^3 and 0.6%ID/cm^3 for [^{64}Cu]-EDTA and [^{64}Cu]-*f*-GO-thin, respectively). Overall the total amounts retained in major organs were almost double for [^{64}Cu]-*f*-GO-thick compared to [^{64}Cu]-*f*-GO-thin, on the other hand [^{64}Cu]-EDTA control sample was almost completely eliminated from the body 3.5 h after injection (Table S2).

4. Discussion

The starting GO material synthesized was of high purity and either single or few-layer thick sheets, as described previously [27,32]. Chemical functionalization of these sheets resulted in *f*-GO-thin, and almost doubling in thickness (to about 5 nm) made of more stacked sheets. Despite this increase in thickness, the material can still be considered within the thin graphene-based material range [36]. Increase in nanosheet thickness after chemical functionalization of GO materials has been previously observed linking different moieties and using different functionalization strategies. We have also previously reported that the chemical functionalization and covalent attachment of DOTA onto the GO surface resulted in increased thickness [27]. Yang et al. reported slight increase in thickness of GO upon covalent functionalization with polyethylene

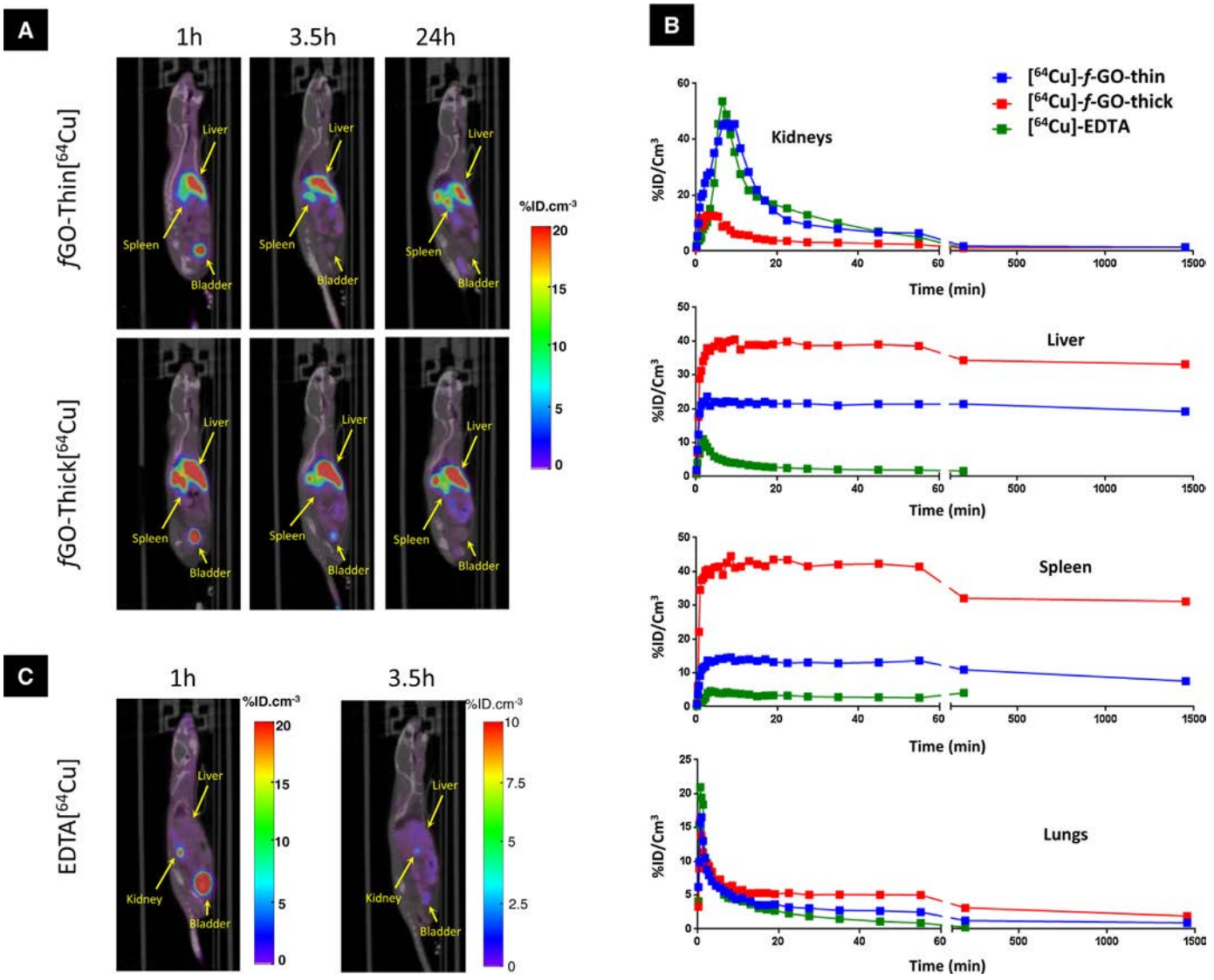

Fig. 2. Dynamic PET/CT imaging and tissue distribution of [^{64}Cu]-*f*-GO-thin, [^{64}Cu]-*f*-GO-thick and [^{64}Cu]-EDTA. (A) Whole body PET/CT images of C57BL/6 mice injected intravenously with [^{64}Cu]-*f*-GO-thin (top) and [^{64}Cu]-*f*-GO-thick (bottom) at different time points (1, 3.5, 24 h); (B) Time activity curves of major organs of C57BL/6 mice injected with [^{64}Cu]-*f*-GO-thin, [^{64}Cu]-*f*-GO-thick and control [^{64}Cu]-EDTA; (C) Whole body PET/CT images of a C57BL/6 mouse injected intravenously with the control sample [^{64}Cu]-EDTA showing almost complete excretion and no tissue accumulation after 3 h. 3-D whole body PET/CT imaging videos can be found in Supplementary data.

glycol (PEG), however a more profound increase (~5 fold) in thickness was detected upon the physisorption of the PEG moiety [21]. Li et al. also demonstrated that the covalent attachment of PEG to GO doubled flake thickness, while the physisorption of bovine serum albumin (BSA) onto GO increased the thickness dramatically by ten-fold [37]. In contrast, lateral size distribution was reduced by GO functionalization, presumably due to further processing (filtration, purification) as has been previously reported for different types of chemistries [37]. The Raman spectra demonstrated the characteristic G band at 1595 cm^{-1} due to bond stretching of sp^2 hybridized carbon atoms and the prominent disorder D band was at 1330 cm^{-1}. The 2D band near 2700 cm^{-1} was absent, and the D to G band intensity ratio (I_D/I_G), corresponding to the metric of disorder [38] in the graphitic structure, increased upon functionalisation as reported before [27]. Furthermore, it increased upon aging due to increased surface defects and disorder with the re-stacking of the sheets. The *f*-GO-thin sheets aged by re-stacking, leading to significant differences in the thickness between the freshly synthesized (*f*-GO-thin) and the same material after aging (*f*-GO-thick). Such re-stacking was irreversible even after long sonication times. Some studies have demonstrated that multi-layered GO films are metastable species, with their structure and surface chemistry evolving at room temperature undergoing reduction [39]. Another study demonstrated that aging of GO resulted in the oxygen functionalities to agglomerate and form highly oxidized domains surrounded by areas of pristine graphene. This was suggested as a means to control the material properties and produce new forms of GO [40]. The latter two studies could explain the re-stacking we observed with our *f*-GO during aging. Despite this significant increase in the thickness of the aged material, the lateral size distribution of the sheets remained largely unchanged.

Both thin (freshly synthesized *f*-GO) and thick (aged *f*-GO) contained the appending DOTA chelating group, capable of complexing radiometals with high efficiency and thermodynamic and kinetic stability as is widely used in clinical nuclear medicine and imaging [33]. The efficiency of [^{64}Cu] radiolabeling of the *f*-GO-thin was more than double that of the *f*-GO-thick (62.7% *vs* 26.4%), likely due to the observed re-stacking of the aged sheets. This resulted in fewer DOTA moieties available for chelation of the isotope [^{64}Cu], and an overall dramatic reduction in radiolabeling efficiency for

the thicker material. However, we did not observe any differences in the stability of radiolabeling once the radiometal complexed with the DOTA moieties. Dynamic PET/CT imaging revealed the blood kinetics and tissue distribution profile for the two radiolabeled *f*-GO materials intravenously injected in anesthetized mice, to show three processes taking place: (a) rapid elimination of the GO material from the blood pool, as previously published [27]; (b) extensive glomerular filtration, bladder accumulation and eventual urinary excretion of the GO flakes within the first few hours after administration; and (c) retention mainly in the liver, spleen and significantly less in the lungs. The latter has been previously reported for other GBMs, including GO [30], but not using PET/CT. The observation of extensive urinary excretion of the material is in agreement to previous studies by us and others using *f*-GO [24–27] (*e.g.* dextran-functionalized graphene) [26]. However, further studies will need to be performed before generalizations are reached with regards to the pharmacological profile of other GBMs.

Elimination of agents injected in the human body is in most cases one of the requirements set by the Food and Drug Administration (FDA) for the development of therapeutic and diagnostic agents. Without clearance or biodegradation into benign products long-term accumulation is considered a potential risk [41–43]. Renal clearance is preferred for imaging contrast agents since it is commonly a rapid elimination process with minimal cellular internalization and no needed for metabolic processing of the material. Most of the current FDA-approved imaging contrast agents exhibit renal clearance efficiency of at least 50% of injected dose within the first 24 h [44]. The size of nanoparticles (NPs) or molecules (drug/toxin) in general has been the main determinant of renal clearance. NPs with small dimensions are excreted *via* the renal pathway due to their capability to cross the glomerular filtration threshold (GFT) < 40 nm [45] or some report even less GFT < 10 nm [41]. Examples of such NPs include quantum dots (QD) [41,46], gold NPs (GNPs) [47–49], silica NPs [50], iron oxides [51], carbon dots [52], copper NPs [53], palladium (Pd) nanosheets [54] and graphene nanosheets [24–26]. The effect of charge and surface coating has been studied to a limited extent, however zwitterionic-coated NPs such as cysteine coated QDs [41], glutathione coated GNPs [49] and glutathione coated Pd nanosheets exhibited high resistance to protein binding thus retained their small dimensions and were more efficiently cleared compared to their charged counterparts. Cationic, small NPs (Ø = 6–8 nm) have been associated with a greater capacity for excretion compared to the anionic ones with similar size, due to the greater chance of interaction with the negatively charged glomerular filtration membrane [42,43]. The total 24 h urinary excretion rate reported for the NPs that are capable of renal passage is generally > 50%, that is within the FDA-approved imaging contrast agents range [44]. NP shape has also been shown to impact renal clearance. The excretion of fibre-shaped carbon nanotubes, despite having one dimension exceeding several times the GFT, has been attributed to their capability to align perpendicularly to the glomerular filtration membrane, and translocate the barrier [45,55].

In the present study, the tissue distribution and urinary excretion of two planar-structured *f*-GO with different thickness distributions were studied. The study revealed the rapid urinary elimination (76.9% of injected dose after 24 h) and less overall (remaining whole-body) accumulation of the thin [^{64}Cu]-*f*-GO-thin material. This may be due to more *in vivo* flexibility [6] of the thinner 2D sheets and their ability to translocate [56] and cross the glomerular filtration barrier to a greater extent compared to the structurally more complex [^{64}Cu]-*f*-GO-thick. This material accumulated in the liver and spleen to a much larger extent, presumably because of increased thickness and rigidity. The lack of renal accumulation or entrapment observed in this study is another promising advantage over other smaller sized NPs that tend to accumulate in the glomerular compartments for longer periods of time increasing the risk of nephrotoxicity [44,47,57]. The ability of sheet-like *f*-GO material to be excreted through the kidney with remarkable efficiency and kinetics is considered promising for various potential therapeutic and imaging applications.

To conclude, in this study, freshly synthesized chemically functionalized, few-layered GO sheets (*f*-GO-thin) and their aged thicker equivalent (*f*-GO-thick) with appending DOTA moieties were radiolabeled and imaged using PET/CT. This allowed us to quantitatively compare the previously unexplored pharmacological profile of *f*-GO materials of different thickness distributions. Our findings indicated that the thinner *f*-GO flakes were able to be excreted *via* the renal pathway to a larger extent compared to thicker *f*-GO. These findings reveal GO sheet thickness as a critical structural feature that will significantly impact pharmacological and eventually toxicological outcomes.

Acknowledgments

The authors thank Nigel Hodson from the Bio-AFM facility (Centre for Tissue Injury and Repair at the University of Manchester) for assistance and advice with the AFM instrumentation. We also would like to thank Patrick Hill from the University of Manchester and Geoff Parr from University of Salford for their assistance with the SEM.

This work was partly supported by the Centre National de la Recherche Scientique (CNRS) by the Agence Nationale de la Recherche (ANR) through the LabEx project Chemistry of Complex Systems (ANR-10-LABX-0026_CSC), and by the International Center for Frontier Research in Chemistry (icFRC). This work was partially supported by the EU 7th RTD Framework Programme, Graphene Flagship project (FP7-ICT-2013-FET-F-604391) and the Wolfson Molecular Imaging Centre (University of Manchester). The author would also like to thank the personnel of the Wolfson Molecular Imaging Centre, and particularly Ms Alison Smigova and Ms Lidan Christie for their technical assistance.

Appendix A. Supplementary data

Supplementary data associated with this article can be found, in the online version, at http://dx.doi.org/10.1016/j.apmt.2016.04.003.

References

[1] A.K. Geim, Graphene: status and prospects, Science 324 (5934) (2009) 1530–1534.
[2] K.S. Novoselov, Nobel lecture: graphene: materials in the flatland*, Rev. Mod. Phys. 83 (3) (2011) 837–849.
[3] K.S. Novoselov, et al., A roadmap for graphene, Nature 490 (7419) (2012) 192–200.
[4] K. Kostarelos, K.S. Novoselov, Graphene devices for life, Nat. Nanotechnol. 9 (10) (2014) 744–745.
[5] D. Bitounis, H. Ali-Boucetta, B.H. Hong, D.-H. Min, K. Kostarelos, Prospects and challenges of graphene in biomedical applications, Adv. Mater. 25 (16) (2013) 2258–2268.
[6] Y. Pan, N.G. Sahoo, L. Li, The application of graphene oxide in drug delivery, Expert Opin. Drug Deliv. 9 (11) (2012) 1365–1376.
[7] K.V. Krishna, C. Ménard-Moyon, S. Verma, A. Bianco, Graphene-based nanomaterials for nanobiotechnology and biomedical applications, Nanomedicine 8 (10) (2013) 1669–1688.
[8] H. Shen, L. Zhang, M. Liu, Z. Zhang, Biomedical applications of graphene, Theranostics 2 (3) (2012) 283–294.
[9] K.P. Loh, Q. Bao, G. Eda, M. Chhowalla, Graphene oxide as a chemically tunable platform for optical applications, Nat. Chem. 2 (12) (2010) 1015–1024.
[10] L. Feng, Z. Liu, Graphene in biomedicine: opportunities and challenges, Nanomedicine 6 (2) (2011) 317–324.
[11] A.C. Ferrari, et al., Raman spectrum of graphene and graphene layers, Phys. Rev. Lett. 97 (18) (2006) 187401.
[12] A. Bendali, et al., Purified neurons can survive on peptide-Free graphene layers, Adv. Healthcare Mater. 2 (7) (2013) 929–933.

[13] Y. Liu, X. Dong, P. Chen, Biological and chemical sensors based on graphene materials, Chem. Soc. Rev. 41 (6) (2012) 2283–2307.
[14] A. Servant, et al., Graphene-based electroresponsive scaffolds as polymeric implants for on-demand drug delivery, Adv. Healthcare Mater. 3 (8) (2014) 1334–1343.
[15] K. Kostarelos, K.S. Novoselov, Exploring the interface of graphene and biology, Science 344 (6181) (2014) 261–263.
[16] J.H. Liu, et al., Effect of size and dose on the biodistribution of graphene oxide in mice, Nanomedicine 7 (12) (2012) 1801–1812.
[17] J.-H. Liu, et al., Biocompatibility of graphene oxide intravenously administrated in mice-effects of dose, size and exposure protocols, Toxicol. Res. 4 (1) (2015) 83–91.
[18] X. Zhang, et al., Distribution and biocompatibility studies of graphene oxide in mice after intravenous administration, Carbon 49 (3) (2011) 986–995.
[19] G. Qu, et al., The ex vivo and in vivo biological performances of graphene oxide and the impact of surfactant on graphene oxide's biocompatibility, J. Environ. Sci. 25 (5) (2013) 873–881.
[20] H. Ali-Boucetta, et al., Purified graphene oxide dispersions lack in vitro cytotoxicity and in vivo pathogenicity, Adv. Healthcare Mater. 2 (3) (2013) 433–441.
[21] K. Yang, et al., In vivo biodistribution and toxicology of functionalized nano-graphene oxide in mice after oral and intraperitoneal administration, Biomaterials 34 (11) (2013) 2787–2795.
[22] L. Yan, et al., Can graphene oxide cause damage to eyesight? Chem. Res. Toxicol. 25 (6) (2012) 1265–1270.
[23] A. Schinwald, F.A. Murphy, A. Jones, W. MacNee, K. Donaldson, Graphene-based nanoplatelets: a new risk to the respiratory system as a consequence of their unusual aerodynamic properties, ACS Nano 6 (1) (2011) 736–746.
[24] K. Yang, et al., In vivo pharmacokinetics long-term biodistribution, and toxicology of PEGylated graphene in mice, ACS Nano 5 (1) (2011) 516–522.
[25] K. Yang, et al., Graphene in mice: ultrahigh in vivo tumor uptake and efficient photothermal therapy, Nano Lett. 10 (9) (2010) 3318–3323.
[26] S. Zhang, K. Yang, L. Feng, Z. Liu, In vitro and in vivo behaviors of dextran functionalized graphene, Carbon 49 (12) (2011) 4040–4049.
[27] D.A. Jasim, C. Ménard-Moyon, D. Begin, A. Bianco, K. Kostarelos, Tissue distribution and urinary excretion of intravenously administered chemically functionalized graphene oxide sheets, Chem. Sci. 6 (7) (2015) 3952–3964.
[28] M.C. Duch, et al., Minimizing oxidation and stable nanoscale dispersion improves the biocompatibility of graphene in the lung, Nano Lett. 11 (12) (2011) 5201–5207.
[29] L. Ma-Hock, et al., Comparative inhalation toxicity of multi-wall carbon nanotubes, graphene, graphite nanoplatelets and low surface carbon black, Part. Fibre Toxicol. 10 (1) (2013) 23.
[30] C. Bussy, D.A. Jasim, N. Lozano, D. Terry, K. Kostarelos, The current graphene safety landscape—a literature mining exercise, Nanoscale 7 (15) (2015) 6432–6435.
[31] A.T. Murdock, et al., Controlling the orientation edge geometry, and thickness of chemical vapor deposition graphene, ACS Nano 7 (2) (2013) 1351–1359.
[32] D.A. Jasim, N. Lozano, K. Kostarelos, Synthesis of few-layered, high-purity graphene oxide sheets from different graphite sources for biology, 2D Mater. 3 (2016) 014006.
[33] J.K. Sosabowski, S.J. Mather, Conjugation of DOTA-like chelating agents to peptides and radiolabeling with trivalent metallic isotopes, Nat. Protoc. 1 (2) (2006) 972–976.
[34] H. Boutin, et al., 18F-GE-180: a novel TSPO radiotracer compared to 11C-R-PK11195 in a preclinical model of stroke, Eur. J. Nucl. Med. Mol. Imaging 42 (3) (2015) 503–511.
[35] E. Kaiser, R.L. Colescott, C.D. Bossinger, P.I. Cook, Color test for detection of free terminal amino groups in the solid-phase synthesis of peptides, Anal. Biochem. 34 (2) (1970) 595–598.
[36] P. Wick, et al., Classification framework for graphene-based materials, Angew. Chem. Int. Ed. 23 (30) (2014) 7714–7718.
[37] Y. Li, et al., Surface coating-dependent cytotoxicity and degradation of graphene derivatives: towards the design of non-toxic, degradable nano-graphene, Small 10 (8) (2013) 1544–1554.
[38] A.C. Ferrari, Raman spectroscopy of graphene and graphite: disorder, electron–phonon coupling, doping and nonadiabatic effects, Solid State Commun. 143 (1–2) (2007) 47–57.
[39] S. Kim, et al., Room-temperature metastability of multilayer graphene oxide films, Nat. Mater. 11 (6) (2012) 544–549.
[40] S. Zhou, A. Bongiorno, Origin of the chemical and kinetic stability of graphene oxide, Sci. Rep. 3 (2013) 2484.
[41] H.S. Choi, et al., Renal clearance of nanoparticles, Nat. Biotechnol. 25 (10) (2007) 1165–1170.
[42] M. Longmire, P.L. Choyke, H. Kobayashi, Clearance properties of nano-sized particles and molecules as imaging agents: considerations and caveats, Nanomedicine 3 (5) (2008) 703–717.
[43] J. Liu, M. Yu, C. Zhou, J. Zheng, Renal clearable inorganic nanoparticles: a new frontier of bionanotechnology, Mater. Today 16 (12) (2013) 477–486.
[44] M. Yu, J. Zheng, Clearance pathways and tumor targeting of imaging nanoparticles, ACS Nano 9 (7) (2015) 6655–6674.
[45] L. Lacerda, et al., Dynamic imaging of functionalized multi-walled carbon nanotube systemic circulation and urinary excretion, Adv. Mater. 20 (2) (2008) 225–230.
[46] H.S. Choi, et al., Design considerations for tumour-targeted nanoparticles, Nat. Nanotechnol. 5 (1) (2010) 42–47.
[47] X.D. Zhang, et al., In vivo renal clearance, biodistribution, toxicity of gold nanoclusters, Biomaterials 33 (18) (2012) 4628–4638.
[48] C. Zhou, M. Long, Y. Qin, X. Sun, J. Zheng, Luminescent gold nanoparticles with efficient renal clearance, Angew. Chem. Int. Ed. 50 (14) (2011) 3168–3172.
[49] R. Hong, et al., Glutathione-mediated delivery and release using monolayer protected nanoparticle carriers, J. Am. Chem. Soc. 128 (4) (2006) 1078–1079.
[50] A.A. Burns, et al., Fluorescent silica nanoparticles with efficient urinary excretion for nanomedicine, Nano Lett. 9 (1) (2009) 442–448.
[51] Z. Zhou, et al., Engineered iron-oxide-based nanoparticles as enhanced T1 contrast agents for efficient tumor imaging, ACS Nano 7 (4) (2013) 3287–3296.
[52] X. Huang, et al., Effect of injection routes on the biodistribution clearance, and tumor uptake of carbon dots, ACS Nano 7 (7) (2013) 5684–5693.
[53] S. Yang, et al., Renal clearance and degradation of glutathione-Coated copper nanoparticles, Bioconjugate Chem. 26 (3) (2015) 511–519.
[54] S. Tang, M. Chen, N. Zheng, Sub-10 nm Pd nanosheets with renal clearance for efficient near-infrared photothermal cancer therapy, Small 10 (15) (2014) 3139–3144.
[55] A. Ruggiero, et al., Paradoxical glomerular filtration of carbon nanotubes, Proc. Natl. Acad. Sci. 107 (27) (2010) 12369–12374.
[56] J. Russier, et al., Evidencing a mask effect of graphene oxide: a comparative study on primary human and murine phagocytic cells, Nanoscale 5 (22) (2013) 11234–11247.
[57] C.H.J. Choi, J.E. Zuckerman, P. Webster, M.E. Davis, Targeting kidney mesangium by nanoparticles of defined size, Proc. Natl. Acad. Sci. 108 (16) (2011) 6656–6661.